PAPER

Check for updates

Multi-layered electrode constructs for neural tissue engineering†

Marjolaine Boulingre, [iD] Mateusz Chodkowski, [iD] Roberto Portillo Lara, [iD] Aaron Lee, [iD] Josef Goding [iD] and Rylie A. Green [iD] *

Although neural tissue engineering holds great therapeutic potential for multiple clinical applications, one important challenge is the development of scaffolds that provide cues required for neural tissue development. To achieve this, biomaterial systems can be leveraged to present appropriate biological, mechanical, topographical and electrical cues that could direct cell fate. In this study, a multi-layered electrode construct was engineered to be used as a platform for 3D cell encapsulation for *in vitro* applications. The first layer is a conductive hydrogel coating, that improves electrical conductivity from the underlying platinum electrode. The second layer is a biosynthetic hydrogel, specifically tailored to support neural development. This layered electrode construct was electrochemically characterised, and a numerical model was applied to study electrical stimuli reaching the biosynthetic hydrogel layer. The construct was shown to effectively support the growth and proliferation of encapsulated astrocytes within the biosynthetic layer, while the numerical model will enable computational experimentation for benchmarking and study validation. This highly versatile system represents a robust tool to study the influence of electrical stimuli on neural fate, as well as investigating the development of biohybrid interfaces *in vitro*.

1. Introduction

Neurological disorders remain among the most challenging causes of long-term disability to treat. To address this need, a broad range of technologies have been developed to replace lost functions or promote tissue repair. Neural tissue engineering relies on the use of biomaterials as scaffolds that guide cell proliferation and differentiation for therapeutic applications. For example, nerve guidance conduits have been developed to promote axonal regeneration following peripheral nerve injury.[1] Biomaterials are also being developed to augment cell-based therapies for neurodegenerative or neurological conditions, such as Parkinson's disease or stroke.[2] As neurons are electrically excitable and their survival depends on electrical stimuli, conductive biomaterials and exogenous electrical stimulation have both been explored to improve neural tissue development and function. Given the remarkable diversity within the nervous system, the establishment of standardised environments that support specific cell phenotypes *in vitro* is key to understand fundamental aspects of neural development and function in both health and disease.

As cells perceive and respond to several physicochemical cues from the environment, an ideal scaffold should replicate the properties of native tissues to ensure adequate growth and development. *In vitro* models have largely relied on cell monolayers grown on stiff plastic substrates. However, these conditions fail to recapitulate the complexities of cell-to-cell and cell-to-ECM interactions, as well as key biomechanical and biochemical properties of living tissues.[3] As a result, monolayer cultures have gradually been replaced by more complex 3D systems where cells are encapsulated in biomimetic scaffolds.[4] Moreover, biomaterial scaffolds allow the combined delivery of several physicochemical stimuli, including mechanical, topographical, and electrical cues. Therefore, multiple biomaterials have been engineered to guide cell proliferation and differentiation towards driving the formation of functional neuronal networks.[5,6]

Hydrogels have emerged as an ideal biomaterial to develop scaffolds for cell culture.[7] Hydrogels are characterised by their hydrated and permissive polymer structures, as well as their highly tuneable properties such as mechanical stiffness, swellability and biodegradability. Synthetic materials such as poly(vinyl)alcohol (PVA) or poly(ethylene glycol) (PEG) have been used to engineer tissue engineering scaffolds owing to the ability to readily modify their mechanical properties.[7] Hydrogels have also been fabricated using biopolymers of natural origin, as they present intrinsic bioinstructive cues such as cell attachment or biodegradable motifs.[6,8] For instance, hydrogel collagen-based scaffolds allow cells to remodel the matrix due to the presence of matrix metalloproteinase

Department of Bioengineering, Imperial College London, South Kensington, London, UK. E-mail: rylie.green@imperial.ac.uk

† Electronic supplementary information (ESI) available. See DOI: **https://doi.org/10.1039/d4tb02651a**

3390 | *J. Mater. Chem. B*, 2025, **13**, 3390–3404

This journal is © The Royal Society of Chemistry 2025

(MMP)-degradable sites. Several studies have shown that material stiffness and viscoelasicity influence neural differentiation and proliferation.[9–12] As the brain is one of the softest tissues and is highly viscoelastic, materials matching these mechanical properties have been developed to leverage mechanoregulatory pathways involved in neural phenotype.[13,14] Similarly, scaffold architecture and topography have been shown to influence an array of cellular mechanisms.[15] Topographical cues have been integrated within scaffolds to direct the elongation of neuronal processes. For instance, anisotropic grooves, aligned fibres or channels at the scaffold surface have been shown to promote oriented cell contact guidance to assist axonal growth.[16] In addition, neural stem cell (NSC) differentiation could also be promoted without negatively impacting cell alignment by modifying fibre diameter of scaffolds.[17]

The spontaneous electrical activity in neurons has been shown to be involved in the development of cortical networks.[18] Over the past few years, there has been a growing interest in the development of conductive substrates for neural tissue engineering.[19,20] The intrinsic conductivity of the substrate has been shown to assist neuronal communication and strengthen newly formed synapses. Conductive scaffolds could also be used to deliver electrical stimulation to encapsulated cells.[21] Multiple studies have shown that electrical stimuli could influence cell development and increase the proliferation and differentiation of neural progenitors.[22–25] Electrical stimuli have also been shown to promote neurite extension both in terms of elongation and orientation. Previous works have also demonstrated that electrically stimulated NSCs cultured on hemin-doped serum albumin-based scaffold exhibit higher differentiation rates and neurite branching.[26] Different conductive elements have been used to establish these types of scaffolds, including gold nanostructures[27,28] and carbon allotropes such as graphene or carbon nanotubes (CNTs).[23,29,30] Conductive polymers (CP) such as poly(3,4-ethylenedioxythiophene) (PEDOT) have also been integrated into hydrogels due to their intrinsic conductive properties. For instance, interpenetrating conducting hydrogel (CH) have been engineered via electropolymerisation of PEDOT inside a PVA hydrogel by covalently functionalising PVA chains with sulphate moieties to act as dopants.[31] In addition, photocrosslinkable CHs containing PEDOT:PSS have been shown to support the differentiation of encapsulated dorsal root ganglion cells.[32]

In vitro platforms that combine hydrogel scaffolds and electrical stimulation have gathered significant research interest towards understanding neural cell development in 3D environments. These approaches have largely relied on direct stimulation via conductive metal electrodes that are submerged in culture medium.[33–35] Despite their ease of use, harmful byproducts can be produced at the electrode–electrolyte interface upon stimulation, and changes in the temperature and pH of the culture medium could potentially lead to cytotoxic effects.[36] Alternatively, electrodes could be located outside the culture well to deliver stimulation via capacitive coupling.[37,38] However, non-uniform electrical fields are generated in these systems as electrode arrangement produces a rectangular or square-shaped electrical field across the circular geometry of

the culture well.[39] This results in limited small cross-section areas exhibiting homogeneous electric fields, which could negatively impact cell development and study replicability. To address this, previous studies have explored the use of circular multi-well culture plates with polymeric microfluidic inserts to generate uniform electric fields.[39] However, the development of culture systems that enable the delivery of electrical stimuli to neural cells maintained in biomimetic 3D environments remains technically challenging. Moreover, because of the wide variety of stimulation parameters that may be explored, computational modelling holds great promise to better understand the actual stimuli that are delivered to cells in culture across different studies.[33,40]

In this study, we report the development of a multi-layered hydrogel system composed of a platinum electrode coated with a conductive PVA/PEDOT hydrogel and a cell supportive PVA–gelatin (GEL) biosynthetic hydrogel (BH). This system can be used as a platform for cell encapsulation and electrical stimulation by leveraging the underlying CH and Pt layers. By using the underlying Pt layer as the stimulating electrode and by placing a counter electrode above the Pt surface, a uniform electrical field can be generated across the cross-sectional area of the hydrogel. The system was characterised by electrochemical impedance spectroscopy and an equivalent circuit model was fitted to study the electrical behaviour of the system and to calculate the conductivity of the hydrogel coating. A computational model of the system was built to determine the electric potential distribution within the construct. In addition, the chronic stability of the hydrogel construct and electrode performance were investigated via accelerated ageing equivalent to four months in culture. Lastly, the cytocompatibility of the hydrogel coating was evaluated in vitro using Schwann cells and primary astrocytes encapsulated in the BH layer. This versatile system represents a robust tool to study the influence of electrical stimuli on neural fate, as well as investigating the development of biohybrid interfaces in vitro (Fig. 1).
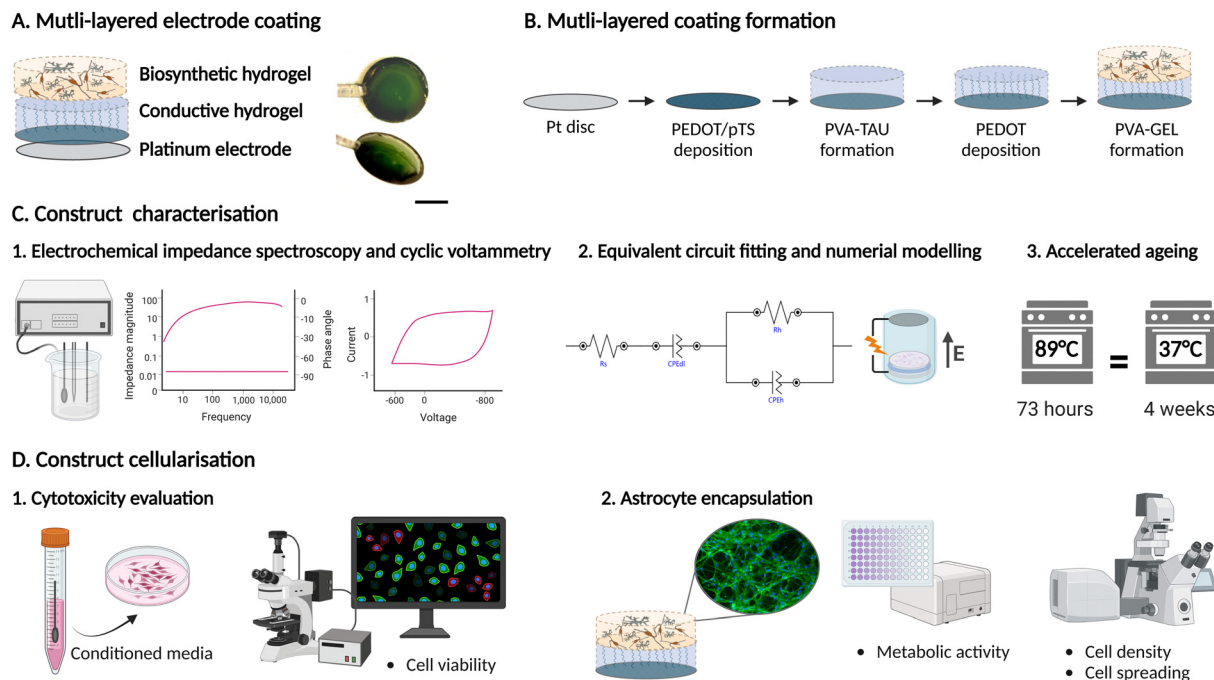
2. Materials and methods

2.1 Production of multi-layered hydrogel coating on Pt electrode

2.1.1 Platinum electrode preparation. Platinum disks of 8 mm in diameter were laser cut from 100 μm thick Pt sheets (99.99% purity, Advent Research Materials). Prior to being coated, the surface of the Pt disks was insulated with medical-grade silicone (NuSil, MED4-4220) to ensure CH deposition was restricted to the electrode site.

2.1.2 CH coating. CH deposition was carried out following previously established protocols.[31] Briefly, a PEDOT/sodium p-toluenesulfonate (pTS) pre-layer was formed on the Pt electrode through galvanostatic electrodeposition using a current density of 1 mA cm^{-2} for 1 min. The precursor solution was composed of 0.1 M 3,4-ethylenedioxythiophene (EDOT) monomer (97% purity, Sigma-Aldrich 483028) and 0.05 M pTS (95% purity, Sigma-Aldrich 152536) dissolved in a solution of

This journal is © The Royal Society of Chemistry 2025

J. Mater. Chem. B, 2025, **13**, 3390–3404 | **3391**

Fig. 1 Fabrication and characterisation of layered electrode constructs. (A) Schematic of the multi-layered electrode construct and representative images of coated Pt electrodes (scale bar = 2 mm). (B) Schematic of the different steps involved in the fabrication of the multi-layered electrode constructs. (C) Constructs were electrochemically characterised using electrochemical impedance spectroscopy and cyclic voltammetry. An electrical equivalent circuit of the multi-layered coating was derived, and a numerical model was developed to obtain the electrical field distribution. Accelerated ageing was performed to assess construct stability. (D) The cytocompatibility of the construct was evaluated using primary rat astrocytes 3D encapsulated within the biosynthetic hydrogel layer. (Figure created with https://BioRender.com.)

deionised water and acetonitrile (Sigma-Aldrich, 34851) mixed in a volumetric ratio of 1:1. Next, a PVA hydrogel was formed on top of the pre-coated Pt disk. PVA (M_w 13 000–23 000, Sigma-Aldrich 348406) was first functionalised with methacrylate (MA) (2-isocyanatoethyl methacrylate 98% purity, Sigma-Aldrich 477 060) and taurine (Tau) (2-aminoethanesulfonic acid, ≥99% purity, Sigma-Aldrich T0625) as described by Goding *et al.*[31] To form the hydrogel, PVA–MA–Tau was dissolved in deionised water at 10 wt%, and 1 mM Irgacure solution was added to reach a final concentration of 0.1 wt%. A glass coverslip was placed on top of the hydrogel precursor to ensure uniform coating thickness, followed by photocrosslinking *via* UV light at an intensity of 30 mW cm^{-2} for 3 min. PEDOT was then polymerised within the PVA–Tau hydrogel network *via* galvanostatic electrodeposition, from an aqueous solution of 0.03 mM EDOT in PBS and applying a current density of 1 mA cm^{-2} for 10 min. Lastly, the CH-coating was dried under laminar flow prior to PVA–GEL deposition. For cell culture experiments, CH-coated electrodes were sterilized in an autoclave at 121 °C for 15 minutes.

2.1.3 PVA–GEL deposition. PVA and gelatin were first functionalised with norbornene (Nb), according to protocols adapted from Qin *et al.*,[41] and Koshy *et al.*[42] respectively. Gelatin and PVA were functionalised with Nb at 20% and 7% degree of substitution, respectively. Briefly, gelatin (Sigma – G1890) was dissolved at 1% w/v in 0.1 M 2-(*N*-morpholino)-ethanesulfonic acid (MES) buffer (pH 6 at 37 °C, Sigma 3671). 5-Norbornene-2-methylamine (TCI N0907) was added at

3 mmol Nb per gram of dry gelatin, before adding NHS (Sigma 130672) and EDC (Sigma 03450) to a molar ratio of 1:3:1 (Nb:EDC:NHS) and reacted for 4 h at 37 °C. The final product was dialysed against deionised water using a 10 kDa MW cutoff cellulose membrane for 3 days, followed by freeze-drying. For PVA functionalisation, PVA and *p*-toluenesulfonic acid (Sigma-Aldrich 40 288-5) were dissolved in anhydrous dimethylsulfoxide (DMSO, Millipore Sigma D4540) under an argon atmosphere at 60 °C. *cis*-5-Norbornene-endo-2,3-dicarboxylic anhydride (Sigma Aldrich 247634) was then added, and the solution was allowed to react for 16 hours at 50 °C under nitrogen atmosphere. The product of the reaction was then dialysed against a 100 mM NaHCO$_3$ solution for 24 hours, followed by 3–4 days of dialysis against deionised water and lyophilisation.

Following polymer functionalisation, PVA–GEL hydrogels were formed following a previously established protocol.[43] Briefly, PVA–Nb and gelatin–Nb were mixed in at 25:75 weight ratio to produce a 10% w/t solution in Dulbecco's phosphate buffer saline (DPBS, Sigma-Aldrich D8537). The crosslinker solution was prepared by dissolving dithiothreitol (DTT, Thermo Scientific™) in DPBS at a thio-to-norbornene stoichiometric ratio of 1:2. Eosin Y was then added to a final concentration of 0.1 mM. The PVA–GEL precursor solution was pipetted on top of the CH-coated electrode followed by photocrosslinking *via* visible light (555 nm) at an intensity of 15 mW cm^{-2} for 3 min.

3392 | *J. Mater. Chem. B*, 2025, **13**, 3390–3404

This journal is © The Royal Society of Chemistry 2025

2.2 Electrochemical characterisation

Electrochemical characterisation was carried out using an Auto-lab potentiostat and the Autolab NOVA software (Metrohm). A three-electrode configuration consisting of the coated Pt disk as the working electrode (WE), a 1 mm diameter Pt wire counter electrode (CE), and an Ag/AgCl reference electrode (RE) was used. Measurements were conducted in PBS.

Electrochemical impedance spectroscopy (EIS) was per-formed from 1 Hz to 10 kHz at 10 points per decade upon applying an AC sinusoid with a peak-to-peak amplitude of 30 mV. Bode plots and Nyquist plots were extracted from the EIS measurements for further analysis.

Cyclic voltammetry (CV) was evaluated by sweeping the voltage between -0.6 V and -0.8 V at a scan rate of 0.15 V s^{-1} and measuring the current response over six cycles. The charge storage capacity (CSC) was obtained by integrating the current response with respect to time and was normalised to the geometric area of the electrode.

2.3 Equivalent circuit modelling

Nyquist plots were extracted from EIS measurements and used to fit an equivalent circuit model using the Autolab NOVA software. The commands 'Electrochemical circle fit' and 'Fit and simulation' were used to derive an equivalent circuit and extract the component values of the circuit. The maximum number of iterations was set to 300, and the fitting was set to stop after 50 repetitions without improvement. The same equivalent circuit was fitted to 8 measurements and the obtained component parameters were averaged to determine their final values. From this, the overall impedance and con-ductivity of the CH–BH-coating were evaluated.

2.4 COMSOL modelling

A physical finite element model (FEM) of the system was generated using the COMSOL Multiphysics software. An axi-symmetric 2D model was created, where the WE consisted of a Pt disk coated with the hydrogel layer. The return electrode consisted of a loop-shaped Pt wire and both electrodes were submerged in cell culture medium. Table 1 shows the dimen-sions of the geometrical elements that were used in the model, as well as the electrical properties of the materials used. The electrical properties were determined from the literature.[44,45] For the layered CH–BH, the conductivity was derived from the equivalent circuit model at 1 kHz. For the simulation, the bottom surface of the Pt plate was designated as the stimula-tion source, and the Pt ring as ground. A 1 V input electric potential was applied to the model, and the response of the system was simulated with a stationary study.

2.5 Accelerated ageing

Accelerated ageing of the CH–BH-coated electrode was carried out at high temperature to an equivalent time of 4 months. Electrodes were immersed in PBS supplemented with 1% penicillin–streptomycin (P/S) (Gibco^{TM} 15140122) and kept in the oven at 89 °C. The equivalent time of polymeric samples

Table 1 Properties of the different components of the COMSOL model of the CH–BH-coated electrode. The hydrogel coating conductivity was reported under the complex form, where j corresponds to the imaginary component

Element	Dimensions	Material	Conductivity, σ [S m^{-1}]
Platinum electrode	$R = 4$ mm $h = 0.1$ mm	Platinum	9.4×10^6
Hydrogel coating	$R = 4$ mm $h = 0.5$ mm	CH–BH	$0.261 + 0.005j$
Counter electrode	$R_{wire} = 0.25$ mm $R_{loop} = 4$ mm	Platinum	9.4×10^6
Culture medium	$R = 6$ mm $h = 5.6$ mm	DMEM	1.4

undergoing accelerated ageing was calculated according to ASTM F1980-21 using eqn (1), where $Q_{10} = 2.0$ and corresponds to the accelerated ageing factor.[46–48]

$$t_{37} = t_{89} \times Q_{10}^{(T-37/10)} \tag{1}$$

EIS and CV measurements were recorded at multiple timepoints.

2.6 Schwan cell culture

Schwan cells (SCL4.1/F7) were cultured in Dulbecco's Modified Eagle's Medium (DMEM) (Gibco^{TM}, D5546) supplemented with 10% (v/v) foetal bovine serum (FBS) (Gibco^{TM}) and 1% (v/v) P/S.[49] For cytotoxicity assays, cells were seeded at 10 000 cells per cm^2 in a 24-well plate and grown in 750 μL of supplemented media. Cells were passaged at 80% confluency, every 7 days and were used up to passage 16.

2.7 Primary astrocyte culture

Primary astrocytes were isolated from the hippocampus of Sprague Dawley rat neonates (P4) following previously estab-lished protocols.[50,51] Pups were euthanised *via* lethal injection of barbiturate and the brains were then excised and dissected to harvest the hippocampal formation. The tissue was digested in 0.025% (v/v) trypsin–EDTA (Gibco), and mechanically dis-sociated with a 1 mL pipette tip, followed by a 200 μL tip. The resulting single cell suspension was passed through a cell strainer with a 40-μm mesh size to remove larger cell aggre-gates. Cells were then plated in poly-L-lysine (PLL) (Sigma-Aldrich P4707)-coated flasks. Cells were seeded at a density of 35 000–40 000 cells per cm^2 and grown in DMEM/F12 (Gibco^{TM} 31330), supplemented with 1% (v/v) P/S, 1% (v/v) FBS and 2% (v/v) B27 (Gibco^{TM}, 17504044). The medium was changed every 2 to 3 days. After 10 days of culture, cultures were passaged and astrocytes were isolated *via* magnetically active cell sorting (MACS, Miltenyi Biotec). Briefly, cells were incubated for 15 min at 4 °C in MACS buffer solution (0.5%) (w/v) bovine serum albumin (BSA) (Fisher Scientific BP9703) in PBS, supplemented with 0.5 mM ethylenediaminetetraacetic acid (EDTA) (Sigma-Aldrich E9884) and anti-glutamate aspartate transporter 1 (GLAST) biotin (ACSA-1, Miltenyi Biotec). Cells were then washed and incubated for 15 min in MACS buffer and anti-biotin MicroBeads (Miltenyi Biotech). Labelled cells were

This journal is © The Royal Society of Chemistry 2025

J. Mater. Chem. B, 2025, **13**, 3390–3404 | **3393**

passed through the magnetic column and the GLAST$^+$ fraction was collected and seeded at a density of 20 000 cells per cm^2 in PLL-coated T75 flasks. Cells were used between the second and sixth passage (P2–P6).

2.8 Primary astrocyte encapsulation

For encapsulation in the BH, astrocytes were added to the PVA–GEL macromer solution dissolved in DPBS at a density of 5×10^6 cells per mL. PVA–GEL hydrogels were formed on CH-coated electrodes *via* photopolymerisation, as described previously. As a control, astrocytes were encapsulated in PVA–GEL hydrogels formed using 6-mm PDMS circular moulds on glass coverslips. After encapsulation, cells were grown in DMEM/F12 supplemented with 1% (w/v) BSA and 1% (v/v) G5 (Gibco^{TM}, 17503012). 50% of the culture medium was refreshed every 3 days and samples were maintained *in vitro* for 14 days before being fixed for staining.

2.9 Cytotoxicity assay

Conditioned medium was prepared by incubating CH–BH-coated electrodes at 37 °C for 24 h. 24 h post-seeding, Schwann cell culture medium was fully replaced with conditioned medium. A commercial live/dead (Invitrogen^{TM} L3224) assay was performed 24 hours after addition of the conditioned medium, following instructions from the manufacturer. Briefly, cells were washed with PBS before being incubated for 30 min in the staining solution composed of PBS supplemented with ethidium homodimer-1 (1 : 500) and calcein AM (1 : 2000). At the end of the incubation, cells were washed with PBS and fresh culture medium was added for imaging. Samples were imaged with an inverted Leica SP8 confocal microscope. Three representative images per sample were taken with the 20× objective (NA 0.75) at 512 × 512 pixels, for 3 biological replicates. Fluorophores were simultaneously excited at 494 nm and 528 nm.

2.10 Alamar blue assay

Cell viability within the construct was determined after 3 and 14 days in culture using a commercial AlamarBlue^{TM} assay (ThermoFisher Scientific DAL1025). On the day of the assay, culture medium was replaced with medium supplemented with 10% (v/v) AlamarBlue^{TM} reagent. After 4 hours of incubation, fluorescence intensity was measured with a Varioskan plate reader at 544 nm excitation and 590 nm emission with an acquisition time of 100 ms.

2.11 Immunofluorescent staining

After 14 days in culture, samples were fixed with 4% (v/v) *para*-formaldehyde (PFA) in PBS for 20 min at room temperature (RT). Samples were washed twice with DPBS and incubated in permeabilisation buffer (deionised water supplemented with sucrose, sodium chloride, magnesium chloride, HEPES buffer and Triton X-100) for 5 min at RT. Samples were then blocked with 5% (w/v) BSA in DPBS for 4 hours at RT and incubated for 2 hours at RT in staining solution with Hoechst 33342 (1 : 1000, ThermoFisher Scientific 62249) and phalloidin-Alexa Fluor^{TM} 488 (1 : 100, Invitrogen A12379) in PBS. The samples were then

washed 3 times with DPBS for 10 min. PVA–GEL hydrogels were removed from the electrodes and placed on a glass-bottom Petri dish for imaging (Cellvis D35-20-1.5H). Images were taken with a Leica SP8 inverted confocal microscope with a fixed scan of 1024 × 1024 pixels. On average, three *z*-stacks were taken per sample at 20× magnification (NA 0.75). Fluorophores were excited at 405 nm and 488 nm, with sequential scans. Frame averaging was applied to enhance signal-to-noise ratio (an average of 2 frames per image).

2.12 Image analysis

Images were processed and analysed using the ImageJ software (National Institutes of Health, United States) and Matlab (Release 2024b, The MathWorks, Inc., Natick, Massachusetts, United States). Results from the live/dead assay were analysed using a macro automated algorithm, and cell proliferation and viability were calculated. Fluorescence micrographs were analysed using Matlab. Fluorescence data was separated by channel and a Gaussian filter was applied for noise reduction. When quantifying nuclear staining, the brightness was adjusted, and the background removed before applying a watershed function. The number of nuclei was quantified and divided by the image area to obtain the cell density. Actin staining was analysed by applying a specific threshold and the resulting expression was divided by the cell count to obtain the average expression per cell.
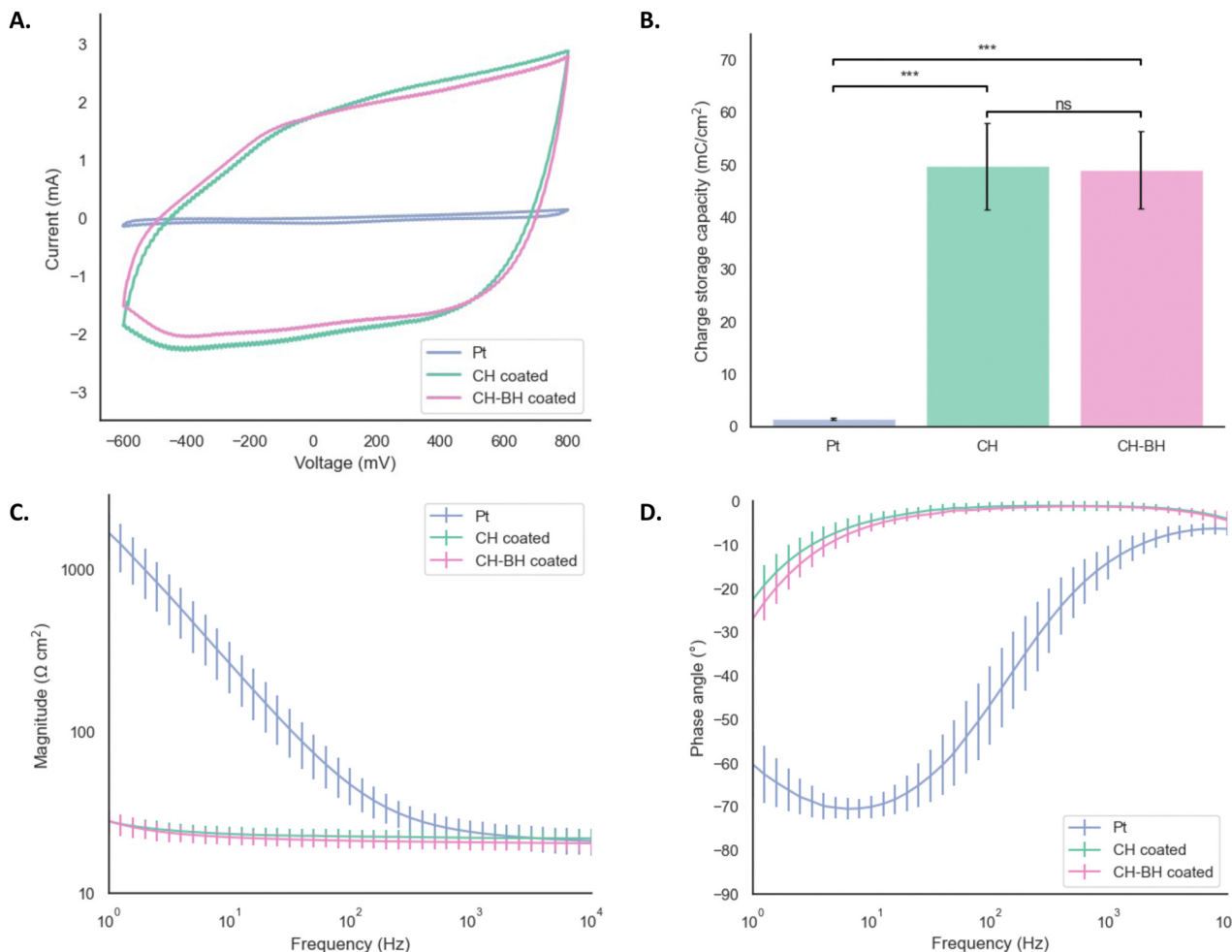
2.13 Statistical analysis

Statistical analysis was conducted using Python 3.8 with SciPy. The results are expressed as the mean ± the standard deviation of the mean. Normality of the datasets was assessed using the Shapiro-Wilk test, and the equality of variance was determined with Levene's test. For normally distributed datasets with equal variance, differences between groups were tested using independent *t*-tests. In the case the datasets were not normally distributed, a Mann–Whitney U test was performed to assess differences between datasets. Differences were considered significant at a significance level of 5% (*: p-value < 0.05), 1% (**: p-value < 0.01) or 0.1% (***: p-value < 0.001).

3. Results and discussion

3.1 Morphological and electrochemical characterisation

Visual inspection of coated Pt electrodes showed proper adhesion of the PVA–TAU hydrogel following deposition of the PEDOT/pTS pre-layer (Fig. 1A), which was due to the increase in surface roughness and mechanical entanglement between polymer chains. A sequential approach was adopted to ensure proper adhesion of the BH to the underlying CH-coated electrodes, which were dried prior to forming the biosynthetic layer. The PVA–GEL precursor was used to re-hydrate the CH before cross-linking to reduce the risk of coating delamination. As there is no chemical reaction that enables attaching both hydrogels together, the different layers can easily separate from each other due to low interfacial adhesion. By rehydrating the CH with the PVA–GEL precursor, the polymer chains of the

3394 | *J. Mater. Chem. B*, 2025, **13**, 3390–3404

This journal is © The Royal Society of Chemistry 2025

Fig. 2 Electrochemical characterisation of CH–BH-coated electrodes. (A) Average representative cyclic voltammogramms of the different layers comprising the electrode construct. (B) CSC of the different layers, determined from the CV. (C) Impedance magnitude and (D) phase angle of the different layers of the electrode construct. Error bars represent the SD of the mean (n = 8).

latter can penetrate the CH layer and allow for physical entanglement of the polymer chains. During polymerisation, the interpenetrating chains become mechanically interlocked with the underlying hydrogel, increasing the adhesion strength between gel layers.

The electrochemical properties of the electrode were measured at each step of the coating process to assess how the different layers influenced the properties of the electrode. CV was used to study the electroactivity of the coated electrode. Current hysteresis curves of Pt, CH-coated and CH–BH-coated electrodes were obtained (Fig. 2A). The CV curve of CH-coated and CH–BH-coated electrodes showed a characteristic box shape, highlighting the presence of pseudocapacitive processes.[10] No significant redox peaks were observed, indicating the absence of unwanted redox reactions. This is relevant in the context of cell stimulation, as redox reactions can lead to the generation of byproducts that can negatively affect cell viability.[52] The charge storage capacity (CSC) of the electrodes was calculated (Fig. 2B), which showed that the CSC of Pt increased more than 30-fold after addition of the CH (from 1.51 ± 0.232 mC cm^{-2} for Pt to

52.65 ± 5.33 mC cm^{-2} for CH-coated Pt). This observation was in accordance with previous studies.[31,53] The addition of the BH did not have a significant impact on the CSC, with a non-significant reduction of 1.53% compared to the CH-coated electrode. The CSC remained more than 30-fold higher than bare Pt electrode.

EIS was used to study the frequency-dependent impedance of the system. The impedance magnitude was calculated over the range of frequencies studied, which showed that both CH-coated and CH–BH-coated electrodes exhibited reduced impedances compared to Pt alone (Fig. 2C). At 1 kHz, the impedance modulus of bare Pt was 47.58 ± 8.35 Ω cm^{-1} and 43.78 ± 5.40 Ω cm^{-1} for CH-coated electrodes. These results were in accordance with previous studies on CH-coated Pt electrodes.[31,53] The addition of the PVA–GEL hydrogel on top of the CH did not significantly change the impedance magnitude of the CH-coated electrode. The phase of both CH-coated and CH–BH-coated electrodes was close to zero for frequencies from 10 Hz to 10 kHz. This was indicative of a dominant resistive behaviour, which is favourable for tissue stimulation as it prevents the build-up of charge at the electrode–tissue interface.[54]

This journal is © The Royal Society of Chemistry 2025

J. Mater. Chem. B, 2025, **13**, 3390–3404 | **3395**

Hydrogels have high swelling behaviour and the aqueous phase allows ion ingress and diffusion of charged ionic species when immersed in ionic solutions.[55–57] Therefore, although the PVA–GEL does not exhibit intrinsic conductivity, charged ionic species are able to move through the matrix resulting in robust electrochemical properties. Moreover, a previous study by Green *et al.* reported a 24.59% increase in the CSC of CH-coated electrodes after the addition of an overlying PVA hydrogel.[58] The CH layer in this construct enables charge transduction from electronic current in metals to ionic current within living tissues.[59] in addition, the hydrogel layer enables safer stimulation by decreasing the current or voltage thresholds required for stimulation.[53,60] This reduces the risk of irreversible faradaic reactions at the electrode–electrolyte interface, which could lead to the generation of toxic byproducts such as reactive oxygen species.[61]

3.2 Equivalent circuit modelling

An equivalent circuit of the hydrogel-coated electrode was derived by analysing the characteristic shapes from the Nyquist plot (Fig. 3). Both CH-coated and CH–BH-coated electrodes were analysed, and a similar circuit was derived for both hydrogel coatings. The circuit consisted of: (1) a series resistor (R_s) that represented the resistance of the electrolyte in which the sample is submerged, (2) a constant phase element (CPE$_{dl}$) that represented the double-layer, and (3) a parallel resistance (R_h) and constant phase element (CPE$_h$) that reflected the resistive and capacitive properties of the bulk hydrogel layer.

Fig. 3 Equivalent circuit fitting of CH–BH-coated electrodes. (A) Equivalent circuit model for the hydrogel-coated electrode where (1) R_s represents the resistance of the electrolyte solution, (2) CPE$_{dl}$ represents the double-layer, and (3) the parallel R_h and CPE$_h$ reflects the resistive and capacitive properties of the hydrogel. Nyquist plot and results of the equivalent circuit model for (B) CH-coated and (C) CH–BH-coated electrode.

A CPE was chosen instead of a pure capacitor to account for the non-ideal behaviour of the system, by reflecting the porosity or roughness of the surface at the interface.[62] The parameters calculated by the fitting for both CH- and CH–BH-coated electrodes are shown on Table 2. The CH–BH coating exhibited higher capacitance compared to the CH coating, as shown by the increase in Q_h and the reduction in n_h. This could be explained by the larger volume of the coating, allowing the polymer network to store more charge.

From the equivalent circuit, the overall impedance of both hydrogel constructs could be derived using eqn (2). To focus solely on the hydrogel coating, the resistance of the solution was omitted from the impedance calculations. At 1 kHz, the real part of the impedance was found to be 42.58 Ω for the CH-coated electrode, and 38.09 Ω for the CH–BH-coated one. From the impedance, the conductivity of both the CH and the CH–BH coating was estimated using eqn (3) and found to be 0.234 S m^{-1} and 0.261 S m^{-1}, respectively. These conductivity values were in the same order of magnitude as other CH coated electrodes in the literature.[63–66]

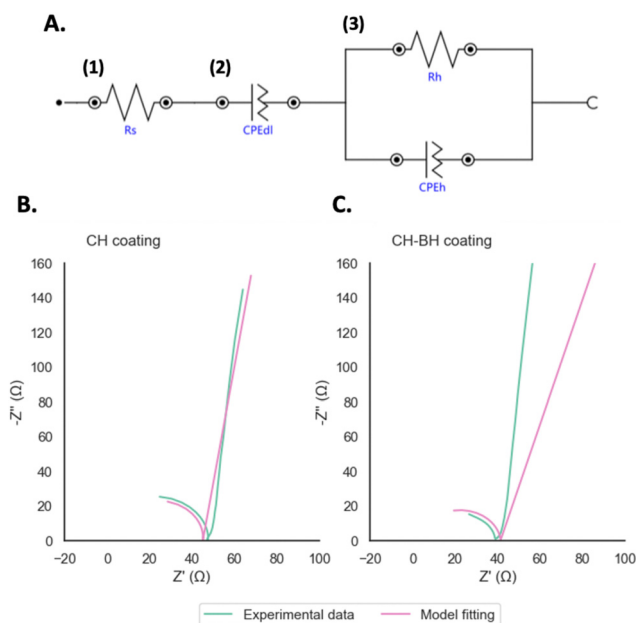$$Z_{electrode} = \frac{R_h}{1 + R_h Q_h (j\omega)^{n_h}} + \frac{1}{Q_{dl}(j\omega)^{n_{dl}}} \quad (2)$$

$$\sigma_{electrode} = \frac{d}{Z_{electrode}A} \quad (3)$$

The comparison of equivalent circuit models of CH- and CH–BH-coated electrodes provided more insight on the influence of the non-conductive BH coating. No statistically significant differences were observed between the conductivities of the two coatings, which further supported the observations from the EIS and CV analysis (Fig. 2). The similarity in the equivalent circuit and the obtained conductivity values suggested that the CH and BH hydrogels could be approximated as a single hydrogel layer.

PBS was used as the electrolyte solution for the measurements, instead of the culture medium used for cell maintenance. However, PBS and physiological medium have similar osmotic and ionic strengths, resulting in similar ionic mobility. Moreover, PBS has a conductivity ranging from 1.35 and 1.70 S m^{-1}, while that of culture medium ranges between 1.4 S m^{-1} [45] and 1.61 S m^{-1}.[67] This similarity between conductivities is therefore not expected to change the overall impedance behaviour of the system.

As the hydrogel coating incorporates a CP, charge can move both within the solid phase along the CP chain, as well as in the aqueous phase by permeating within the hydrogel mesh. Therefore, an alternative model that accounts for the porous structure of the resulting coated electrode and combines both electronic and ionic conduction could have also been derived, such as that reported by Onnela *et al.*[68] Similarly, each individual hydrogel could also be modelled by a CPE and a resistance placed in parallel, while the final layered construct could be represented by placing these two parallel branches in series. However, this approach would not replicate the system accurately, as the two hydrogels are not physically separated but

3396 | *J. Mater. Chem. B*, 2025, **13**, 3390–3404

This journal is © The Royal Society of Chemistry 2025

Table 2 Parameters of the components of the fitted models of CH- and CH–BH-coated electrodes

| Layer	R_s [Ω]	Q_{dl} [mF s^{-1} (n_{dl}^{-1})]	n_{dl}	R_h [Ω]	Q_h [nF s^{-1} (n_h^{-1})]	n_h
CH	2.56 ± 7.54	9.88 ± 1.29	0.91 ± 0.02	42.56 ± 10.45	16.65 ± 13.38	1.05 ± 0.05
CH–BH	3.26 ± 12.00	8.60 ± 1.14	0.83 ± 0.10	38.13 ± 8.18	108.89 ± 149.16	0.94 ± 0.15

rather interconnected to one another. Furthermore, it is likely that the overall conductivity of the system would change following cell encapsulation within the BH layer due to their intrinsic electrical activity. As cells develop within the BH, the gelatin would be digested and the BH would be replaced by the secreted ECM. This in turn would result in scaffold reorganisation and changes in both charge distribution and permeation within the coating. As the complexity of this system would increase with cell development, a simplified model was used to capture key aspects of the initial state and to approximate the CH–BH coating with the parallel resistance and the CPE. This model provided an estimation of the conductivity of the hydrogel coating that could be then integrated into a computational model. Future work could derive more complex models by tracking the evolution of the impedance response before and after cell encapsulation, as well as during cell growth and proliferation.

3.3 COMSOL modelling

The electrical field distribution upon stimulation was simulated on COMSOL to study how the electric field spreads through the hydrogel layers. As mentioned above, the equivalent circuit fitted on the experimental data of the CH–BH-coated electrode has the same components as the model of the CH-only, which suggests that the addition of the BH does not change the electrochemical processes happening within the construct. Furthermore, as there is physical entanglement of both hydrogels, there is no clear boundary between the CH and the BH. Based on this, the multi-layered coating was approximated as one single hydrogel layer in the COMSOL model. The conductivity derived from the equivalent circuit of the CH–BH-coated electrode was used to describe this component in the COMSOL model. A 2D model, symmetric around the z-axis was established, rather than a 3D one. This axisymmetric 2D model allowed to reduce the degrees of freedom and the complexity of the simulations while still representing the system geometry and behaviour.

The magnitude and direction of the electric potential along the cross-section of the system in the YZ-plane was calculated (Fig. 4A). This showed that there is a gradual drop of 44.5% in the intensity of the electric field at the centre as it travels
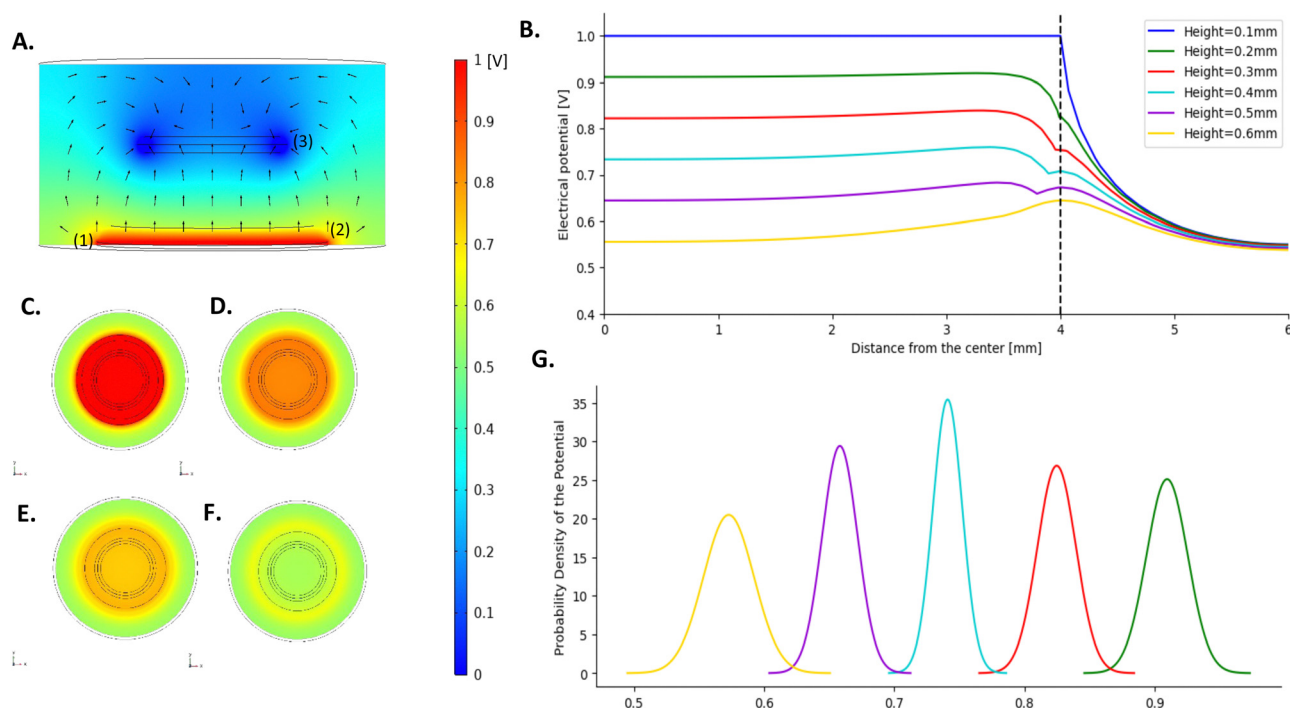
Fig. 4 Numerical model of the voltage distribution within the CH–BH-coated electrode, for 1 V stimulation at 1 kHz. (A) 3D view of the simulation results with the direction of the electric field and magnitude. The chamber represents the electrode in a standard well of a culture plate, submerged in culture medium. The bottom part represents the Pt electrode (1) and the CH–BH-coating (2), while the top part represents the counter electrode (3). (B) Electric potential across the cross-section of the hydrogel coating at different heights. A height of 0.1 mm corresponds to the Pt surface, and a height of 0.6 mm corresponds to the hydrogel–solution interface. Distribution of the electric potential across the coating at the height of (C) 0.1 mm, (D) 0.3 mm, (E) 0.4 mm and (F) 0.6 mm. (G) Probability density distribution of the potential at the cross-section at multiple heights.

through the hydrogel, away from the electrode. This is highlighted in Fig. 4B, which represents a detailed visualisation of the distribution of the electric field across the electrode in the *XY*-plane, for heights ranging from 0.1 mm (platinum electrode surface) to 0.6 mm (hydrogel–electrolyte interface). By calculating the electrical potential across the *XY* plane of the coating at different heights, it was shown that the electrical potential is mostly uniform across the entire surface (Fig. 4C–F). There is however a slight decrease in the potential at the boundary of the hydrogel, with the potential experiencing a boost as it crosses the boundary. This is most likely due to edge effects at the border of the electrode. Such effect is not noticeable at the contact surface of the electrode and its coating, but it becomes more pronounced further away from the electrode. 100 μm away from the Pt electrode, the potential value at the edge of the coating decreases by 9.51%, compared to the potential at the centre. At the highest section of the hydrogel coating (0.5 mm away from the Pt electrode surface) there is a 9.99% increase in the potential at the border compared to the centre. The hydrogel coating is exposed to the electrolyte not only at its upper surface, but also around its circumference. Because of the low impedance of the interface, the electric potential readily extends out of the hydrogel through the sides, creating an uneven distribution of potential across the cross-sectional area, especially at the edges.

The derived model allows the assessment of the spatial variability of the stimulation and to obtain a good understanding of the electrical stimuli that cells undergo within the system. Although a decrease in the electrical potential was noted at the edges of the electrode, the largest part of the construct exhibited homogeneous potential values, with standard deviations less than 0.02 for all the different heights.

To improve the robustness of the studies, the analysis of cell responses to electrical stimuli could be limited to the area where the voltage is homogenous, and the edge of the coating could be excluded from the analysis. If the last 0.2 mm of the circumference of the coating is discarded, it would represent 46.1% of the total cell culture area. This effective surface area of

stimulation is larger than that reported in similar studies.[39] The application of an external electric field induces a series of changes in cells exposed to the stimuli that could promote cell polarization.[69,70] This activates downstream signalling molecules and triggers cytoskeletal changes in an asymmetric manner, which underlies a variety of cellular processes, including directional cell migration (*i.e.*, electrotaxis). Therefore, achieving field uniformity is important to elicit controlled and homogeneous cellular responses and to better understand the impact of electrical stimuli on encapsulated cells *in vitro*.

In this study, the conductivity of the hydrogel coating was derived at 1 kHz and might not be representative of lower frequency stimulation paradigms. However, the overall conductivity of the system is not significantly influenced by the frequency and stays in a similar range for frequencies ranging from 1 Hz to 10 kHz (Fig. S1, ESI†). The conductivity of the coating at 1 Hz was computed to be 0.221 S m^{-1}, representing 84.7% the value at 1 kHz. The simulation was run for this new conductivity and the distribution of the potential was comparable to the first simulation. A higher drop in the potential along the height of the scaffold was nonetheless observed, with a 54.5% decrease in the potential at the centre at the interface between the hydrogel and the medium (Fig. S2, ESI†). This further highlights the utility of having such a model, as it allows to easily visualise the voltage response according to different stimulation paradigms. Furthermore, the parameters of the model can be updated to fit other types of coatings, allowing to be easily applied to other studies.

3.4 Stability under accelerated ageing

The stability of the coating was assessed through accelerated ageing *via* elevated temperature. Samples were kept at 89 °C for 73 hours, to mimic four months of ageing at 37 °C. No delamination was observed during the incubation period. Fig. 5A and B represent the evolution of the impedance magnitude and phase angle. There was a non-significant decrease of 1.25% in the impedance at 1 Hz after the incubation period,
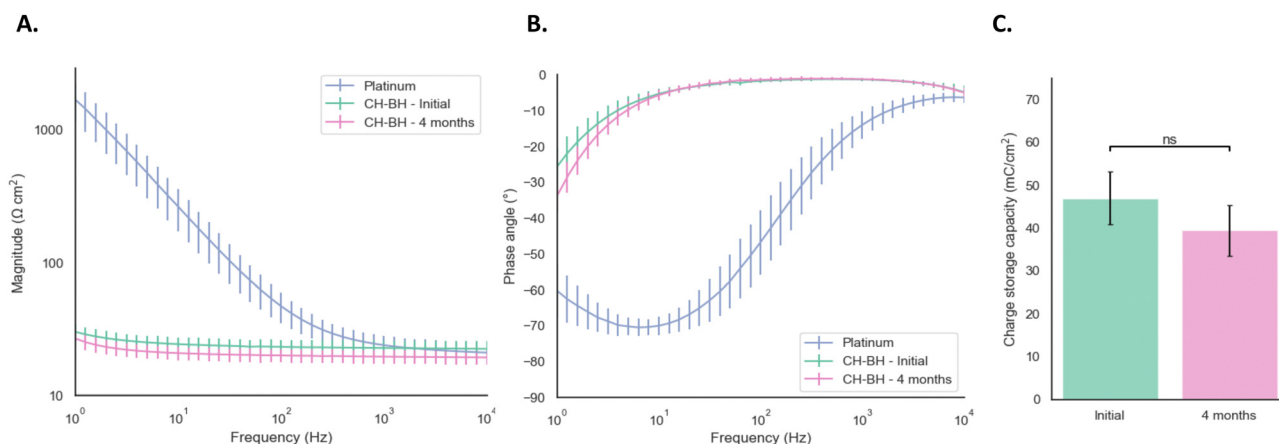

Fig. 5 Electrochemical characterisation of CH–BH-coated electrode pre- and post-accelerated ageing. (A) Impedance magnitude and (B) phase angle of the initial CH–BH-coating and after the equivalent of 4 months of ageing. (C) CSC of the CH–BH-coating before and after ageing. Error bars represent the SD of the mean (*n* = 8).

3398 | *J. Mater. Chem. B*, 2025, **13**, 3390–3404

This journal is © The Royal Society of Chemistry 2025

compared to the initial impedance. The evolution of the CSC over time is shown in Fig. 5C. The maximum loss in CSC corresponded to 1.38% after two months of ageing.

These results were in accordance with previous studies focusing on the long-term electrochemical stability of coated electrodes.

For example, Green *et al.* reported a slow reduction in the CSC of CH-coated stainless steel electrode arrays under accelerated electrochemical ageing through high frequency stimulation.[71] Loss in CH performance can be explained by the fact that these materials undergo chain rearrangements and can lose dopant components over time.[72] However, in the multi-layered coating proposed, the dopant used for the polymerisation of the CP is covalently attached to the polymer backbone, thus reducing the potential loss of dopant over time.

While no delamination of the PVA–GEL was observed during the incubation time, the PVA–GEL hydrogel layer appeared thinner under visual inspection. This behaviour could be explained as the hydrogel is hydrolytically degradable. Previous studies showed that PVA–GEL hydrogels lose up to 30% of their original weight when incubated for 28 days in PBS.[43,73,74] The behaviour of the system will also be influenced by the addition of cells due to the biodegradability of gelatin, which enables cells to remodel the scaffold as they secrete and deposit their own ECM. This dynamic process of cellular remodelling is particularly relevant over extended timelines. The ability of cells to digest the scaffold could lead to an increase in mass swelling and facilitate the movement of ions throughout the matrix, increasing the overall transmission of charge. However, the density and composition of the newly deposited ECM could also influence this response, as the deposition of a thick and dense matrix could limit the permeation of soluble molecules. However, it is anticipated that the electrochemical properties of the CH coating would remain stable over time, allowing robust delivery of stimulation paradigms over long periods of cell culture.

3.5 Cellularised CH–BH-coated electrode

The cytocompatibility of the multi-layered construct was evaluated through indirect contact tests. Schwann cells were grown for 24 h in conditioned medium, which was produced by incubating CH–BH-coated electrodes for 24 h. A commercial live/dead assay was performed to assess the cytocompatibility of the CH–BH coating (Fig. 6). An ethanol gradient was used to induce cell death *via* membrane disruption in samples used as positive controls, and cell density was determined for each condition. Cell viability could not be accurately determined as most of the dead cells were washed away during the staining (Fig. 6A). However, the quantification of cell density showed that higher concentrations of ethanol induced higher rates of cell death, which confirmed the sensitivity and applicability of the assay (Fig. 6B). These results also showed that there was no reduction in cell density after 24 h in conditioned medium, compared to negative controls. Moreover, a 23.1% increase in density was observed for medium conditioned with CH–BH-coated electrodes compared to the tissue culture polystyrene
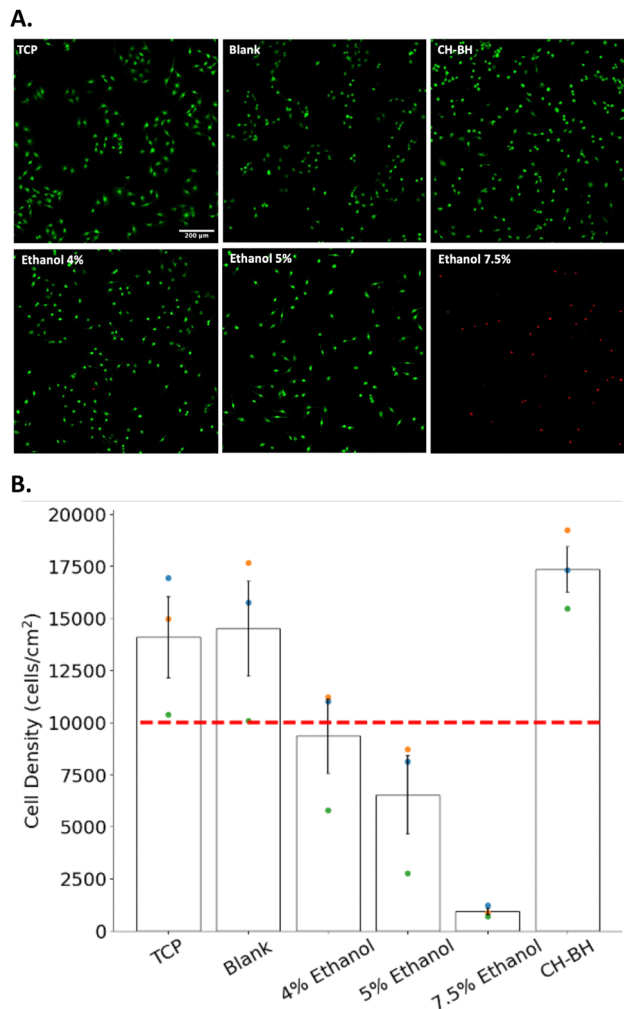
Fig. 6 Cytocompatibility of CH–BH-coated electrodes. (A) Representative fluorescence micrographs of live/dead stained cells (green: live cells stained with calcein–AM, red: dead cells stained with ethidium homodimer, scale bar 200 μm). (B) Quantification of cell density. Cells were seeded at 10 000 cells per cm² (represented by the red line). (TCP: tissue culture polystyrene negative control, blank: fresh culture medium control). Error bars represent the SD of the mean ($n = 9$ for TCP, Blank and ethanol gradient, $n = 27$ for the CH–BH).

(TCP) control. This could be explained in part due to the presence of gelatin in the conditioned media. Since coated electrodes are incubated in media right after crosslinking, unreacted gelatin could have leached out of the construct leading to improved cell attachment and proliferation. Overall, these results demonstrated that the CH–BH-construct did not induce any cytotoxic responses, which confirmed the ability of the system to support the development of encapsulated cells.

After evaluating the cytocompatibility of the CH–BH-coated electrodes using cultures of Schwann cells, primary astrocytes were then encapsulated in the BH layer and grown for 14 days. As a control, cells were also encapsulated in BH hydrogels. An Alamar blue assay was used to evaluate the metabolic activity of cells over the 14 days of culture. This assay relies on the reduction of a non-fluorescent dye (resazurin) to its fluorescent

This journal is © The Royal Society of Chemistry 2025

*J. Mater. Chem. B*, 2025, **13**, 3390–3404 | **3399**

from (resorufin) by metabolically active cells. Changes in metabolic activity were calculated by comparing the fluorescence intensity of the supernatant at day 3 and day 14. These results showed an approximate 41% increase in fluorescence from day 3 to day 14 was observed for both CH–BH and BH scaffolds (Fig. 7B). This in turn further confirmed that the CH does not impact the cytocompatibility of the BH component, and that cells could effectively grow and develop within the layered construct.

To further evaluate cell development in the construct, encapsulated cells were characterised *via* immunofluorescent staining. Cell density was obtained by counterstaining cell nuclei with Hoechst, while staining of actin was used to assess cell morphology (Fig. 7A). As shown in fluorescence micrographs, primary astrocytes were able to develop and spread in stand-alone BHs and CH–BH-coated Pt electrodes. Astrocytes grown in coated electrodes exhibited a 1.5-fold higher cell density, with around 55 000 cells per cm^2 compared to 35 000

cells per cm^2 on stand-alone BHs (Fig. 7C). Average cell spreading was determined from the actin coverage normalised by the cell count and was shown to be similar in both conditions, with around 1400 μm^2 per cell in stand-alone BHs and 1800 μm^2 per cell in coated electrodes (Fig. 7D).

The BH used in this study was specifically tailored for the encapsulation of astrocytes. The gelatin component provides biological cues for cell attachment, such as integrin binding sites, and was already shown to allow astrocyte growth and development.[43] Gelatin also provides enzymatic cleavage sites, allowing cells to digest and remodel the scaffold as they grow and facilitating cell migration within the scaffold. Furthermore, topographical and mechanical cues such as matrix stiffness have been shown to play major roles in cell fate.[75] In this study, astrocytes were shown to migrate and preferentially develop around the stiffer planes of the constructs, located near the underlying glass coverslip for the stand-alone BHs or the Pt disk for the CH–BH-coated electrodes. The electrical properties
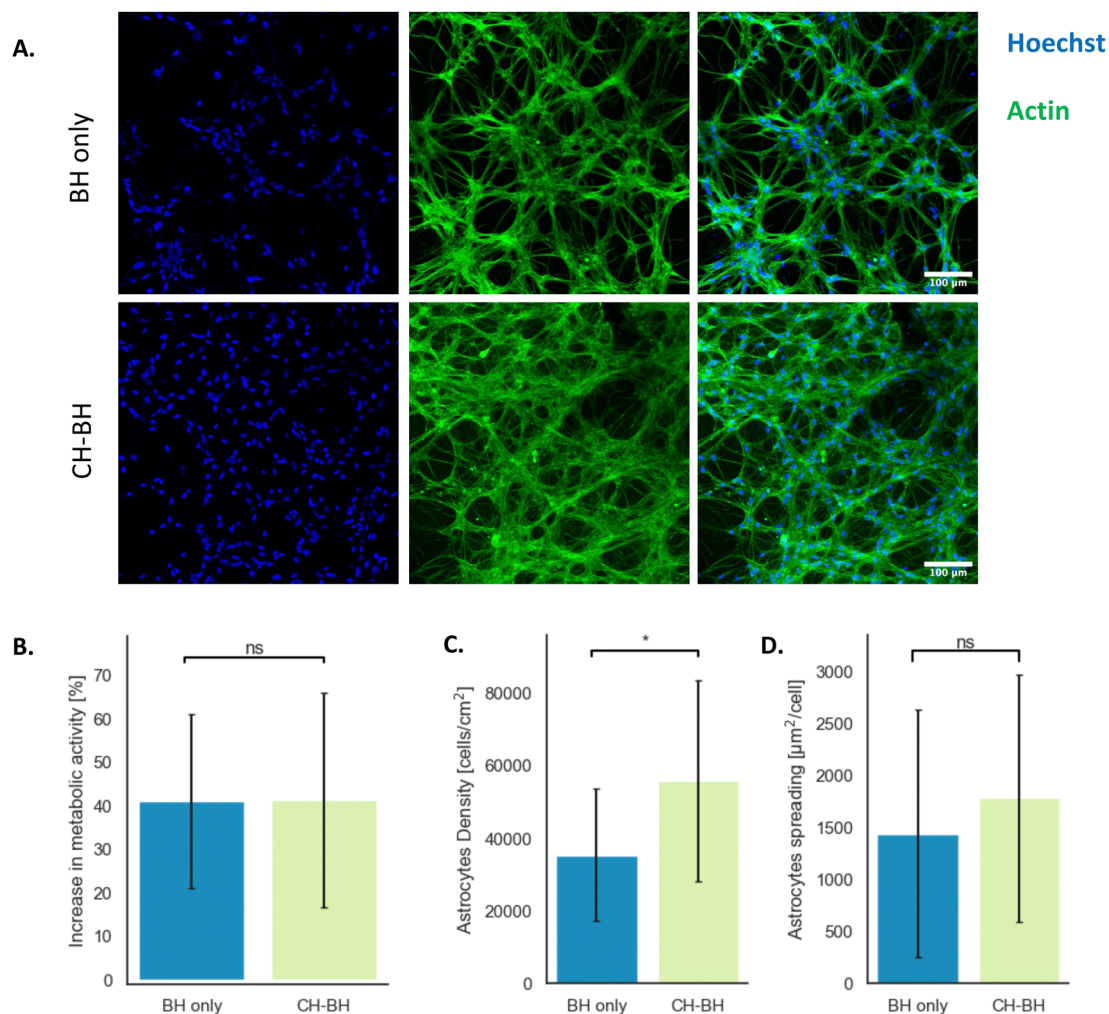
Fig. 7 *In vitro* assessment of cell proliferation and metabolic activity. (A) Representative fluorescence micrographs of primary astrocytes encapsulated in PVA–GEL after 14 days in culture. Scale bar = 100 μm. 20× magnification. (B) Increase in metabolic activity of primary astrocytes encapsulated in BHs or CH–BH constructs after 3 and 14 days of culture. (C) Astrocyte density and (D) spreading in stand-alone BHs and CH–BH-coated electrodes after 14 days in culture. More than 2000 cells were counted over 3 replicates. Error bars represent the SD of the mean.

3400 | *J. Mater. Chem. B*, 2025, **13**, 3390–3404

This journal is © The Royal Society of Chemistry 2025

of biomaterial scaffolds have also been shown to play a major role in cell proliferation and differentiation *in vitro*. For instance, Tringides *et al.*[23] showed an increase in astrocyte density when cell were grown on viscoelastic and conductive scaffolds. Therefore, the underlying CH could enhance cell proliferation in the construct and result in higher cell density near the CH layer. Furthermore, the porous structure of the underlying CH could facilitate the diffusion of nutrients and other soluble molecules across the scaffold leading to improved cell development. However, this behaviour could have also been aided by the delay in crosslinking the BH precursor after casting. Although this was done to improve the interpenetration of the BH and CH, this could also allow cells to sediment and locate at the bottom of the hydrogels.

Overall, this study demonstrated that encapsulated neural cells could effectively develop within the multi-layered hydrogel construct that comprises the electrode coating. These results highlight the potential of this system as a platform to study the effect of electrical cues on cell fate. Electrical stimulation has been widely implemented in multiple cell culture systems to influence cell proliferation, migration or differentiation. The delivery of electrical stimuli can trigger membrane depolarisation and influence the gating of multiple ion channels, thus resulting in changes in intracellular ion concentrations.[76] Calcium is one of the most studied ionic species because of its important role as a secondary messenger in a wide variety of signalling pathways, ultimately influencing gene transcription and protein expression.[77] At more immediate timescales, calcium signalling has also been shown to promote exocytosis of various signalling molecules.[77] Intracellular calcium in astrocytes has been shown to mediate the release of gliotransmitters that modulate the activity of neighbouring cells, such as glutamate or D-serine.[78–80] Therefore, electrical stimuli could be used to selectively control intracellular and extracellular calcium signalling in astrocytes maintained *in vitro*.[81] Electrical stimuli could also directly influence a number of signalling pathways that are involved in cell growth, proliferation or differentiation, such as the MAPK/ERK or PI3K/Akt kinases pathways.[70] Therefore, *in vitro* systems like this hold great promise to increase understanding of electrically mediated mechanisms that underlie neural cell development in both health and disease. Moreover, the multilayered design of the electrode construct provides multiple advantages to study the development of bioelectronic interfaces *in vitro*.

4. Conclusions

In this study, a multi-layered hydrogel electrode coating was developed. The layered assembly was shown to be stable for up to an equivalent of 4 months of ageing. The underlying CH layer improved the electrochemical properties of the Pt electrode, by reducing the impedance and increasing the CSC. An equivalent circuit model enabled the characterisation of the conductivity of the engineered coating. A COMSOL model was developed to investigate how electrical stimuli propagate within the different layers of the coating. This COMSOL model constitutes a valuable tool to visualise the electrical potential perceived by cells encapsulated in the construct, and it could be used more broadly to facilitate comparisons across different studies. The cytocompatibility of the construct was assessed using cultures of Schwann cells, and primary astrocytes encapsulated within the BH layer were shown to be able to effectively grow and develop within the scaffold. Future work will explore the ability of the construct to support the development of different cell phenotypes to assess the impact of electrical stimuli on a variety of cellular processes. For instance, co-cultures of primary neural progenitors and astrocytes will be used to explore the influence of electrical stimulation on neuronal differentiation, neurite extension and synaptic network formation.

The biosynthetic hydrogel used in this study provides high versatility, as it could be readily modified to accommodate a variety of electroactive cell types, such as bone,[82] cartilage[83] and muscle.[84] The biosynthetic layer could also be tailored to encapsulate mesenchymal stem cells to evaluate the effect of electrical stimuli on the differentiation into specific lineages, such as osteoblasts and chondrocytes. The layered design of this system would also allow the study of cell alignment or migration with respect to exogenous electric fields.[85] Similarly, the impact of electrical stimuli on myocyte maturation or cardiomyocyte alignment has gathered significant interest in the field of cardiac tissue engineering.[86,87] Therefore, this platform not only holds significant promise for fundamental studies, but also for a variety of translational applications in orthopaedic or cardiovascular research.

Owing to the multi-layered design of the hydrogel construct, this system could be also used to study the development of different bioelectronic interfaces. In particular, the biological layer between the electrode substrate and the target tissue recapitulates the organisation of biohybrid interfaces. These types of devices rely on tissue-engineered components to improve their biological integration into the surrounding host tissues.[88,89] Therefore, this system could be used as a model to study the complex and dynamic processes that underlie the development of biohybrid technologies. Moreover, the ability to deliver electrical stimuli to the construct could be leveraged to investigate the influence of stimulation paradigms on the maturation and biointegration of the interface prior to *in vivo* assessment.

In summary, the high versatility, modularity, and scalability of this multi-layered construct underscore the potential of this platform to develop bespoke electrode systems for a variety of applications in fundamental and translational research.

Author contributions

MB designed the study. MB collected and analysed the experimental data and MC developed the computational models. MB wrote the manuscript with editing by MC, RPL, AL, JG and RG.

This journal is © The Royal Society of Chemistry 2025

J. Mater. Chem. B, 2025, **13**, 3390–3404 | **3401**

All authors approved the final version of the manuscript. Funding was obtained by RG.

Data availability

The datasets generated during and/or analysed during the current study are not publicly available due to ethics and IP but are available from the authors on reasonable request.

Conflicts of interest

There are no conflicts to declare.

Acknowledgements

References

1 L. M. Marquardt and S. E. Sakiyama-Elbert, *Curr. Opin. Biotechnol*, 2013, **24**, 887–892.

2 K. F. Bruggeman, N. Moriarty, E. Dowd, D. R. Nisbet and C. L. Parish, *Br. J. Pharmacol.*, 2019, **176**, 355–368.

3 D. D. McKinnon, A. M. Kloxin and K. S. Anseth, *Biomater. Sci.*, 2013, **1**, 460–469.

4 K. Duval, H. Grover, L.-H. Han, Y. Mou, A. F. Pegoraro, J. Fredberg and Z. Chen, *Physiology*, 2017, **32**, 266–277.

5 E. R. Aurand, K. J. Lampe and K. B. Bjugstad, *Neurosci. Res. Lett.*, 2012, **72**, 199–213.

6 R. Boni, A. Ali, A. Shavandi and A. N. Clarkson, *J. Biomed. Sci.*, 2018, **25**, 90.

7 J. L. Drury and D. J. Mooney, *Biomaterials*, 2003, **24**, 4337–4351.

8 M. C. Catoira, L. Fusaro, D. Di Francesco, M. Ramella and F. Boccafoschi, *J. Mater. Sci.: Mater. Med.*, 2019, **30**, 115.

9 A. Banerjee, M. Arha, S. Choudhary, R. S. Ashton, S. R. Bhatia, D. V. Schaffer and R. S. Kane, *Biomaterials*, 2009, **30**, 4695–4699.

10 A. I. Teixeira, S. Ilkhanizadeh, J. A. Wigenius, J. K. Duckworth, O. Inganäs and O. Hermanson, *Biomaterials*, 2009, **30**, 4567–4572.

11 O. Chaudhuri, L. Gu, D. Klumpers, M. Darnell, S. A. Bencherif, J. C. Weaver, N. Huebsch, H. Lee, E. Lippens, G. N. Duda and D. J. Mooney, *Nat. Mater.*, 2016, **15**, 326–334.

12 O. Chaudhuri, J. Cooper-White, P. A. Janmey, D. J. Mooney and V. B. Shenoy, *Nature*, 2020, **584**, 535–546.

13 J. M. Barnes, L. Przybyla and V. M. Weaver, *J. Cell Sci.*, 2017, **130**, 71–82.

14 J. M. Stukel and R. K. Willits, *Tissue Eng., Part B*, 2016, **22**, 173.

15 D. Hoffman-Kim, J. A. Mitcel and R. V. Bellamkonda, *Annu. Rev. Biomed. Eng.*, 2010, **12**, 203–231.

16 D. Kim, S.-M. Kim, S. Lee and M.-H. Yoon, *Sci. Rep.*, 2017, **7**, 7716.

17 F. Yang, R. Murugan, S. Wang and S. Ramakrishna, *Biomaterials*, 2005, **26**, 2603–2610.

18 R. Shi and R. B. Borgens, *Dev. Dyn.*, 1995, **202**, 101–114.

19 A. Burnstine-Townley, Y. Eshel and N. Amdursky, *Adv. Funct. Mater.*, 2020, **30**, 1901369.

20 J. H. Min, M. Patel and W.-G. Koh, *Polymers*, 2018, **10**, 1078.

21 C. Bertucci, R. Koppes, C. Dumont and A. Koppes, *Brain Res. Bull.*, 2019, **152**, 265–284.

22 C. L. Weaver and X. T. Cui, *Adv. Healthcare Mater.*, 2015, **4**, 1408–1416.

23 C. M. Tringides, M. Boulingre, A. Khalil, T. Lungjangwa, R. Jaenisch and D. J. Mooney, *Adv. Healthcare Mater.*, 2023, **12**(7), 2202221.

24 C. Barberio, J. Saez, A. Withers, M. Nair, F. Tamagnini and R. M. Owens, *Adv. Healthcare Mater.*, 2022, **11**, 2200941.

25 F. Pires, Q. Ferreira, C. A. V. Rodrigues, J. Morgado and F. C. Ferreira, *Biochim. Biophys. Acta, Gen. Subj.*, 2015, **1850**, 1158–1168.

26 C.-C. Hsu, A. Serio, N. Amdursky, C. Besnard and M. M. Stevens, *ACS Appl. Mater. Interfaces*, 2018, **10**, 5305–5317.

27 K. Baranes, M. Shevach, O. Shefi and T. Dvir, *Nano Lett.*, 2016, **16**, 2916–2920.

28 N. Saderi, M. Rajabi, B. Akbari, M. Firouzi and Z. Hassannejad, *J. Mater. Sci.: Mater. Med.*, 2018, **29**, 134.

29 Z. Zhang, L. H. Klausen, M. Chen and M. Dong, *Small*, 2018, **14**, 1801983.

30 A. N. Koppes, K. W. Keating, A. L. McGregor, R. A. Koppes, K. R. Kearns, A. M. Ziemba, C. A. McKay, J. M. Zuidema, C. J. Rivet, R. J. Gilbert and D. M. Thompson, *Acta Biomater.*, 2016, **39**, 34–43.

31 J. Goding, A. Gilmour, P. Martens, L. Poole-Warren and R. Green, *Adv. Healthcare Mater.*, 2017, **6**, 1601177.

32 D. N. Heo, S.-J. Lee, R. Timsina, X. Qiu, N. J. Castro and L. G. Zhang, *Mater. Sci. Eng., C*, 2019, **99**, 582–590.

33 M. O'Hara-Wright, S. Mobini and A. Gonzalez-Cordero, *Front. Cell Dev. Biol.*, 2022, **10**, 901652.

34 S. Mobini, L. Leppik and J. H. Barker, *Biotechniques*, 2016, **60**, 95–98.

35 K. Srirussamee, R. Xue, S. Mobini, N. J. Cassidy and S. H. Cartmell, *J. Tissue Eng.*, 2021, **12**, 2041731420974147.

36 C. Chen, X. Bai, Y. Ding and I.-S. Lee, *Biomater. Res.*, 2019, **23**, 25.

37 J. S. Khaw, R. Xue, N. J. Cassidy and S. H. Cartmell, *Acta Biomater.*, 2022, **139**, 204–217.

38 R. A. da Silva, R. Xue, S. I. C. de Torresi and S. Cartmell, *Biointerphases*, 2022, **17**, 011001.

39 H.-F. Tsai, J.-Y. Cheng, H.-F. Chang, T. Yamamoto and A. Q. Shen, *Sci. Rep.*, 2016, **6**, 26222.

40 J. Zimmermann, K. Budde, N. Arbeiter, F. Molina, A. Storch, A. M. Uhrmacher and U. van Rienen, *Front. Bioeng. Biotechnol.*, 2021, **9**, DOI: **10.3389/fbioe.2021.765516**.

41 X.-H. Qin, X. Wang, M. Rottmar, B. J. Nelson and K. Maniura-Weber, *Adv. Mater.*, 2018, **30**, 1705564.

3402 | *J. Mater. Chem. B*, 2025, **13**, 3390–3404

This journal is © The Royal Society of Chemistry 2025

42 S. T. Koshy, R. M. Desai, P. Joly, J. Li, R. K. Bagrodia, S. A. Lewin, N. S. Joshi and D. J. Mooney, *Adv. Healthcare Mater.*, 2016, **5**, 541–547.

43 M. Genta, PhD thesis, Imperial College, London, 2023.

44 conductivity platinum – Wolfram|Alpha, **https://www.wolframalpha.com/input?i=conductivity+platinum**, (accessed August 7, 2024).

45 M.-T. Chen, C. Jiang, P. T. Vernier, Y.-H. Wu and M. A. Gundersen, *PMC Biophys.*, 2009, **2**, 9.

46 D. W. L. Hukins, A. Mahomed and S. N. Kukureka, *Med. Eng. Phys.*, 2008, **30**(10), 1270–1274.

47 R. A. Green, R. T. Hassarati, L. Bouchinet, C. S. Lee, G. L. M. Cheong, J. F. Yu, C. W. Dodds, G. J. Suaning, L. A. Poole-Warren and N. H. Lovell, *Biomaterials*, 2012, **33**(25), 5875–5886.

48 Standard Guide for Accelerated Aging of Sterial Barrier Systems and Medical Devices, **https://www.astm.org/f1980-21.html**, (accessed January 24, 2025).

49 SCL 4.1/F7, **https://www.culturecollections.org.uk/nop/product/scl-41f7**, (accessed August 3, 2024).

50 Collagenase-based Single Cell Isolation of Primary Murine Brain Endothelial Cells Using Flow Cytometry, **https://bio-protocol.org/en/bpdetail?id=3092&type=0**, (accessed August 3, 2024).

51 L. Zelenka, D. Pägelow, C. Krüger, J. Seele, F. Ebner, S. Rausch, M. Rohde, S. Lehnardt, K. van Vorst and M. Fulde, *J. Neurosci. Methods*, 2022, **366**, 109420.

52 D. R. Merrill, M. Bikson and J. G. R. Jefferys, *J. Neurosci. Methods*, 2005, **141**, 171–198.

53 R. A. Green, R. T. Hassarati, J. A. Goding, S. Baek, N. H. Lovell, P. J. Martens and L. A. Poole-Warren, *Macromol. Biosci.*, 2012, **12**, 494–501.

54 G. L. Mario Cheong, K. S. Lim, A. Jakubowicz, P. J. Martens, L. A. Poole-Warren and R. A. Green, *Acta Biomater.*, 2014, **10**, 1216–1226.

55 D.-H. Kim, J. A. Wiler, D. J. Anderson, D. R. Kipke and D. C. Martin, *Acta Biomater.*, 2010, **6**, 57–62.

56 J. A. Goding, A. D. Gilmour, U. A. Aregueta-Robles, E. A. Hasan and R. A. Green, *Adv. Funct. Mater.*, 2018, **28**, 1702969.

57 Y. Zhou, C. Wan, Y. Yang, H. Yang, S. Wang, Z. Dai, K. Ji, H. Jiang, X. Chen and Y. Long, *Adv. Funct. Mater.*, 2019, **29**, 1806220.

58 J. Goding, A. Gilmour, U. A. Robles, L. Poole-Warren, N. Lovell, P. Martens and R. Green, *MRS Commun.*, 2017, **7**, 487–495.

59 E. A. Cuttaz, Z. K. Bailey, C. A. R. Chapman, J. A. Goding and R. A. Green, *Adv. Healthcare Mater.*, 2024, **13**, 2304447.

60 R. A. Green, K. S. Lim, W. C. Henderson, R. T. Hassarati, P. J. Martens, N. H. Lovell and L. A. Poole-Warren, in 2013 35th Annual International Conference of the IEEE Engineering in Medicine and Biology Society (EMBC), 2013, pp. 6957–6960.

61 S. F. Cogan, *Annu. Rev. Biomed. Eng.*, 2008, **10**, 275–309.

62 M. Zhou, B. K. Young, E. della Valle, B. Koo, J. Kim and J. D. Weiland, *Sci. Rep.*, 2023, **13**, 6973.

63 Y. Lu, D. Wang, T. Li, X. Zhao, Y. Cao, H. Yang and Y. Y. Duan, *Biomaterials*, 2009, **30**, 4143–4151.

64 V. R. Feig, H. Tran, M. Lee and Z. Bao, *Nat. Commun.*, 2018, **9**, 2740.

65 D. M. Nguyen, Y. Wu, A. Nolin, C.-Y. Lo, T. Guo, C. Dhong, D. C. Martin and L. V. Kayser, *Adv. Eng. Mater.*, 2022, **24**, 2200280.

66 D. M. Nguyen, C.-Y. Lo, T. Guo, T. Choi, S. Sundar, Z. Swain, Y. Wu, C. Dhong and L. V. Kayser, *ACS Polym. Au*, 2024, **4**, 34–44.

67 G. Pucihar, T. Kotnik, M. Kandušer and D. Miklavčič, *Bioelectrochemistry*, 2001, **54**, 107–115.

68 N. Onnela, V. Savolainen, M. Hiltunen, M. Kellomäki and J. Hyttinen, in 2013 35th Annual International Conference of the IEEE Engineering in Medicine and Biology Society (EMBC), 2013, pp. 539–542.

69 T. Taghian, D. A. Narmoneva and A. B. Kogan, *J. R. Soc., Interface*, 2015, **12**, 20150153.

70 Q. Liu and B. Song, *Int. J. Biochem. Cell Biol.*, 2014, **55**, 264–268.

71 N. A. Staples, J. A. Goding, A. D. Gilmour, K. Y. Aristovich, P. Byrnes-Preston, D. S. Holder, J. W. Morley, N. H. Lovell, D. J. Chew and R. A. Green, *Front. Neurosci.*, 2018, **11 zo**, DOI: **10.3389/fnins.2017.00748**.

72 A. N. Dalrymple, M. Huynh, U. A. Robles, J. B. Marroquin, C. D. Lee, A. Petrossians, J. J. Whalen, D. Li, H. C. Parkington, J. S. Forsythe, R. A. Green, L. A. Poole-Warren, R. K. Shepherd and J. B. Fallon, *J. Neural Eng.*, 2019, **17**, 016015.

73 M. Genta, C. Vallejo-Giraldo, J. Goding and R. A. Green, *Tissue Eng., Part A*, 2022, **28**, S244.

74 M. Boulingre, M. Genta, R. Portillo Lara, J. Goding and R. A. Green, *Tissue Eng., Part A*, 2023, **29**, 13–14.

75 J. C. Benincasa, M. I. Madias, R. M. Kandell, L. M. Delgado-Garcia, A. J. Engler, E. J. Kwon and M. A. Porcionatto, *ACS Biomater. Sci. Eng.*, 2024, **10**, 4279–4296.

76 R. Zhu, Z. Sun, C. Li, S. Ramakrishna, K. Chiu and L. He, *Exp. Neurol.*, 2019, **319**, 112963.

77 M. J. Berridge, M. D. Bootman and H. L. Roderick, *Nat. Rev. Mol. Cell Biol.*, 2003, **4**, 517–529.

78 C. Agulhon, J. Petravicz, A. B. McMullen, E. J. Sweger, S. K. Minton, S. R. Taves, K. B. Casper, T. A. Fiacco and K. D. McCarthy, *Neuron*, 2008, **59**, 932–946.

79 V. Parpura and P. G. Haydon, *Proc. Natl. Acad. Sci. U. S. A.*, 2000, **97**, 8629–8634.

80 C. Henneberger, T. Papouin, S. H. R. Oliet and D. A. Rusakov, *Nature*, 2010, **463**, 232–236.

81 R. Fabbri, A. Scidà, E. Saracino, G. Conte, A. Kovtun, A. Candini, D. Kirdajova, D. Spennato, V. Marchetti, C. Lazzarini, A. Konstantoulaki, P. Dambruoso, M. Caprini, M. Muccini, M. Ursino, M. Anderova, E. Treossi, R. Zamboni, V. Palermo and V. Benfenati, *Nat. Nanotechnol.*, 2024, **19**, 1344–1353.

82 L. Leppik, K. M. C. Oliveira, M. B. Bhavsar and J. H. Barker, *Eur. J. Trauma Emerg. Surg.*, 2020, **46**, 231–244.

83 H. J. Kwon, G. S. Lee and H. Chun, *Sci. Rep.*, 2016, **6**, 39302.

84 K. Ronaldson-Bouchard, S. P. Ma, K. Yeager, T. Chen, L. Song, D. Sirabella, K. Morikawa, D. Teles, M. Yazawa and G. Vunjak-Novakovic, *Nature*, 2018, **556**, 239–243.

This journal is © The Royal Society of Chemistry 2025

J. Mater. Chem. B, 2025, **13**, 3390–3404 | **3403**

85 P. Su, Y. Tian, C. Yang, X. Ma, X. Wang, J. Pei and A. Qian, *Int. J. Mol. Sci.*, 2018, **19**, 2343.

86 D. Hernández, R. Millard, P. Sivakumaran, R. C. B. Wong, D. E. Crombie, A. W. Hewitt, H. Liang, S. S. C. Hung, A. Pébay, R. K. Shepherd, G. J. Dusting and S. Y. Lim, *Stem Cells Int.*, 2016, **2016**, 1718041.

87 M. Morsink, P. Severino, E. Luna-Ceron, M. A. Hussain, N. Sobahi and S. R. Shin, *Acta Biomater.*, 2022, **139**, 141–156.

88 A. E. Rochford, A. Carnicer-Lombarte, V. F. Curto, G. G. Malliaras and D. G. Barone, *Adv. Mater.*, 2020, **32**, 1903182.

89 M. Boulingre, R. Portillo-Lara and R. A. Green, *Chem. Commun.*, 2023, **59**, 14745–14758.

3404 | *J. Mater. Chem. B*, 2025, **13**, 3390–3404

This journal is © The Royal Society of Chemistry 2025